Secondary beam fragments produced by 200 MeV u^{-1} ^{12}C ions in water and their dose contributions in carbon ion radiotherapy

2008 New J. Phys. 10 075003

(http://iopscience.iop.org/1367-2630/10/7/075003)

New Journal of Physics
The open-access journal for physics

Secondary beam fragments produced by 200 MeV u^{-1} ^{12}C ions in water and their dose contributions in carbon ion radiotherapy

K Gunzert-Marx[1], H Iwase[2], D Schardt[3] and R S Simon
Gesellschaft für Schwerionenforschung, Planckstr. 1, D-64291 Darmstadt, Germany
E-mail: d.schardt@gsi.de

New Journal of Physics **10** (2008) 075003 (21pp)
Received 10 February 2008
Published 28 July 2008
Online at http://www.njp.org/
doi:10.1088/1367-2630/10/7/075003

Abstract. For applications in heavy-ion radiotherapy, the emission of secondary fragments from 200 MeV u^{-1} carbon ions was investigated using a 12.78 cm thick water absorber as a tissue-equivalent beam stopping target. Secondary light particles (n, p, d, t, ^{3}He and ^{4}He) produced by nuclear fragmentation and emerging from the target in forward direction were detected with a $\Delta E - E$-telescope consisting of NE102 and BaF_2 scintillation detectors. Energy spectra of the fragments at angles of 0°, 5°, 10°, 20° and 30° to the beam axis were obtained from time-of-flight measurements. They show a broad maximum at about half of the projectiles energy per nucleon, the shape at high energies is exponential and extends up to the projectiles initial energy per nucleon—for neutrons and protons to about twice the energy of the projectile per nucleon. Comparison of the experimental data with calculations performed with the Monte-Carlo code (partide and heavy ion transport code system (PHITS)) shows fairly good agreement for neutrons, protons and deuterons, but some deviations for tritons and helium fragments. The neutron dose in patient treatments with carbon ions was estimated to be 8 mGy per treatment-Gy based on the measured neutron yield.

[1] Present address: Siemens Medical Solutions, Particle Therapy, Hofmannstr. 26, D-91052 Erlangen, Germany.
[2] Present address: KEK, Radiation Science, 1-1 Oho, Tsukuba, Ibaraki, 305-0801, Japan.
[3] Author to whom any correspondence should be addressed.

Contents

1. Introduction

The slowing-down process of heavy charged particles in a thick target is governed by continuous interactions with the atomic shell of the target nuclei as described by the Bethe–Bloch formula. The resulting depth-dose profile (Bragg curve) which exhibits a flat plateau region and a distinct peak near to the end of the range of the particles represents the major physical advantage of heavy charged-particle beams in radiotherapy. The additional advantage of an elevated biological effectiveness (relative biological effectiveness (RBE)) in the Bragg peak region makes heavy ions very attractive for the treatment of deep-seated local tumours [1]. This has been confirmed by very promising clinical studies [2, 3] with carbon ions at HIMAC/Chiba and GSI Darmstadt.

At energies of several hundred megaelectronvolts per atomic mass unit which are required for radiotherapy applications, the radiation field is significantly affected by nuclear fragmentation processes with increasing penetration depths. The most frequently occurring nuclear reactions are peripheral collisions where the beam particles may lose one or several nucleons. This process can be described by the abrasion–ablation model [4] as illustrated in figure 1. Nucleons in the overlapping zone of the interacting projectile and target nuclei are abraded and form the hot reaction zone (fireball), whereas the outer nucleons (spectators) are only slightly affected by the collision. In the second step (ablation), the remaining projectile and target fragments as well as the fireball de-excite by evaporating nucleons and light clusters. Those emitted from the projectile fragments appear forward peaked in the laboratory frame

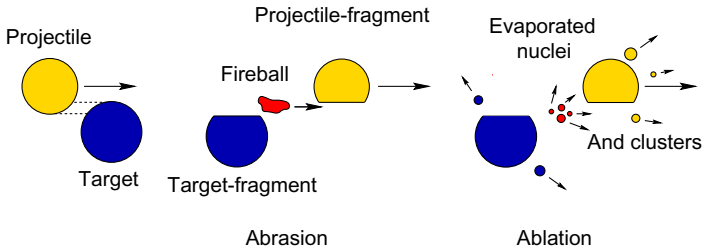

Figure 1. A simplified model of the nuclear fragmentation due to peripheral collisions of projectile and target nucleus as described by Serber [4].

due to the high velocity of the projectile. The projectile-like fragments continue travelling with nearly the same velocity and direction, and contribute to the dose deposition until they are completely slowed down or undergo further nuclear reactions. Neutrons and clusters from target-like fragments are emitted isotropically and with much lower velocities. The particles ablated from the fireball cover the range between the projectile and target emission. Nuclear fragmentation reactions lead to an attenuation of the primary beam flux and a build-up of lower-Z fragments with increasing penetration depth. The lower-Z fragments have longer ranges than the primary ions as the range of particles (at the same velocity) scales with A/Z^2. Therefore, the depth-dose profile of heavy-ion beams shows a characteristic fragment tail beyond the Bragg peak (figure 2).

The physical beam models included in treatment planning programs for heavy-ion irradiations of cancer patients have to take into account these effects and comparison with experimental data is indispensable for the validation process. A particular complication of the dose evaluation arises from the fact that the RBE depends on the nuclear charge Z and the linear energy transfer (LET) of the particles. Therefore, in order to predict the biologically effective dose D_{biol}, the composition of the particle field and the LET-distributions have to be known at each point of the treatment volume:

$$D_{\mathrm{biol}}(\vec{r}) = \sum_{Z=1}^{Z_{\mathrm{P}}} \int_{0}^{E_{\max}} \Phi(Z, E, \vec{r}) \cdot \mathrm{LET}(Z, E) \cdot \mathrm{RBE}(Z, E) \cdot \frac{1}{\rho(\vec{r})}\, \mathrm{d}E. \tag{1}$$

Here Φ denotes the particle fluence, ρ the mass density of the target material (tissue) and the sum is taken over the spectrum of charged particles including the primary ions (Z_{p}) and all lower-Z secondary or higher-order fragments down to protons. The dose contribution of secondary neutrons can be treated similarly by considering their indirect interaction using the KERMA concept or fluence-to-dose conversion factors obtained, e.g. from Monte-Carlo calculations. A detailed description of treatment planning for carbon ion therapy including optimization of the biologically effective dose is given in [7, 8].

First experimental studies of the fragmentation of light ions in water or tissue-substitute materials dedicated to biomedical applications were carried out in 1971 at Princeton [9]. At LBL Berkeley detailed measurements [10] were performed on the characterization of 670 MeV u^{-1} ^{20}Ne beams which were used for patient treatments at the BEVALAC. Further investigations of nuclear fragmentation in water and tissue-substitute materials were carried out at the carbon ion treatment facilities at GSI Darmstadt [11, 12] and at HIMAC in Chiba [13, 14]. All these studies included charged fragments only, whereas experimental data on neutron

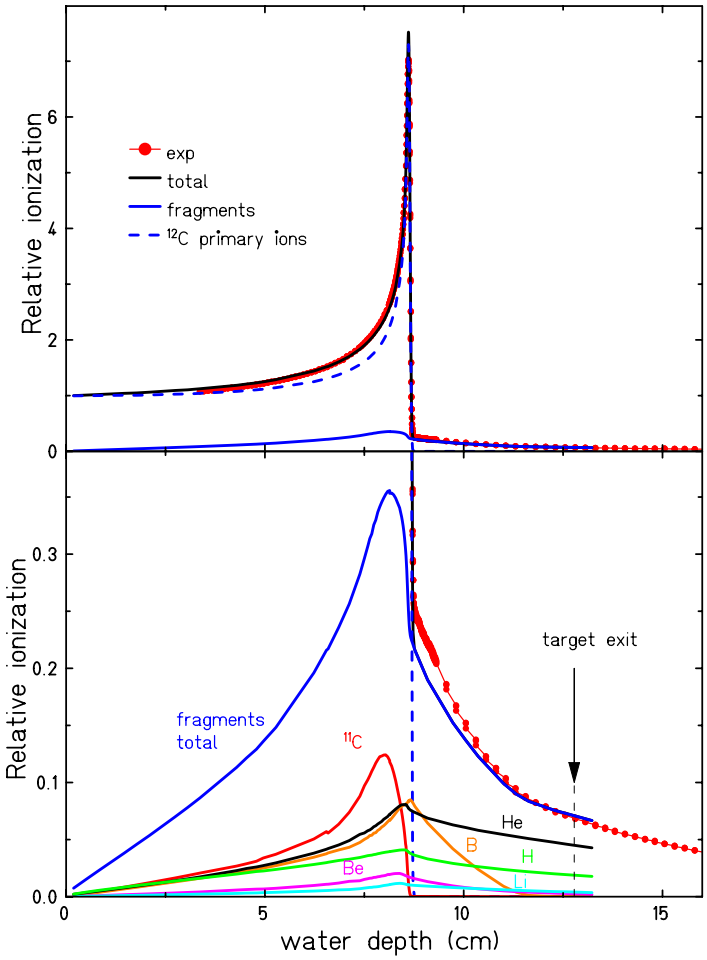

Figure 2. The ionization function (Bragg curve) of a 200 MeV u^{-1} ^{12}C ion beam in water. The measurement was performed with parallel-plate ionization chambers and a precision water absorber [5, 6]. Calculations with the Monte-Carlo code (particle and heavy ion transport code system (PHITS)) (see section 4) are in good agreement with the measurement. The lower part with magnified ordinate scale shows the contribution of fragments with different atomic numbers Z as calculated with PHITS. The thickness of the water target used in our fragmentation measurements is indicated by an arrow.

emission from thick targets relevant for heavy-ion cancer treatment are still scarce. We mention the work by Cecil *et al* [15] on neutron production from 710 MeV alpha particles stopped in water and more recently the work by Kurosawa *et al* [16, 17] and Heilbronn *et al* [18] using ^{12}C and ^{4}He beams stopped in various thick target materials.

In this paper, which is part of a thesis work [19], we report experimental fluence data as well as energy- and angular-distributions of secondary fragments emerging from a thick water target behind the stopping depth of primary carbon ions. A short report of this experiment was presented previously at the NEUDOS-9 conference [20]. The measurements include light charged particles (p, d, t, ^{3}He and ^{4}He) and fast neutrons ($E_n > 20$ MeV) which contribute to the dose tail behind the Bragg peak. The experimental results are compared to simulations using the

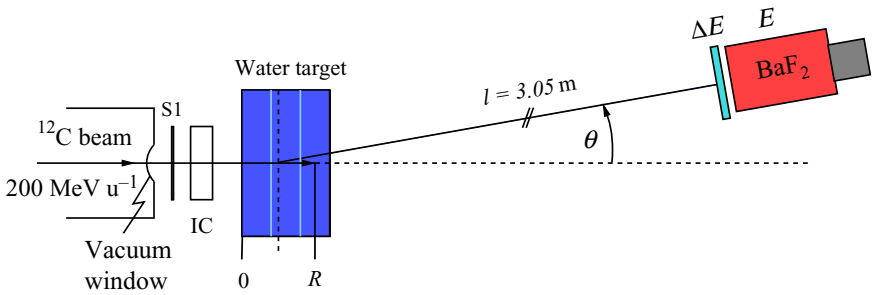

Figure 3. A schematic view of the experimental set-up. The primary ^{12}C ions were stopped in a 12.78 cm thick water target (mean range $R = 8.57$ cm). Secondary fragments emitted from the target in forward direction were identified with a $\Delta E - E$ scintillation telescope placed under various angles θ with respect to the beam axis. The energy of the fragments was obtained from time-of-flight measurements.

Monte-Carlo code PHITS. The energy of the primary carbon ions of 200 MeV u^{-1} represents a mean value of the set of energies typically required for treatments of tumours in the head and neck regions performed at GSI Darmstadt since December 1997.

2. Experimental techniques

2.1. Beam and target characteristics

A sketch of the experimental set-up is shown in figure 3. Carbon ions of 200 MeV u^{-1} were delivered by slow extraction mode from the heavy-ion synchrotron SIS18 at GSI Darmstadt. After passing through a thin vacuum exit window (Hostaphan/Kevlar) the ions were detected by a beam counter (S1) consisting of a 1 mm thick BC400 scintillation paddle with an area of 10×10 cm^2. An air-filled parallel-plate ion chamber (IC) provided an independent check of the number of incoming beam particles for normalization of the fragmentation data. The primary ions were stopped in a 12.78 cm thick water target at a mean range of 8.57 cm calculated by the code ATIMA [21]. The water target consisted of three successive thin-walled rectangular flasks made of optically clear polystyrene. The outer dimensions of each flask were $x = 11.9$ cm, $y = 20.0$ cm and $z = 4.26$ cm, where x and y denote the lateral size and height (both perpendicular to the beam axis), and z the length in beam direction. The material traversed by the beam particles was 3.84 cm water and 0.42 cm polystyrene (entrance and exit wall) for each flask. The total water-equivalent thickness of one flask is 4.265 cm. The central axis (z-coordinate) of the water target was aligned to the centre of the beam axis (see figure 3).

The pencil-like carbon ion beam with approximately Gaussian-shaped horizontal and vertical profiles was focused by two magnetic quadrupole lenses located 10 m upstream the target point to a spot size of about 7 mm full width at half maximum (FWHM) in front of the water target and had a small angular divergence $\sigma_{\text{ang}} \approx 1$ mrad. The beam position and horizontal and vertical profiles were checked with a multi-wire chamber which was inserted in front of the water target, but moved out of the beam during the fragmentation measurements.

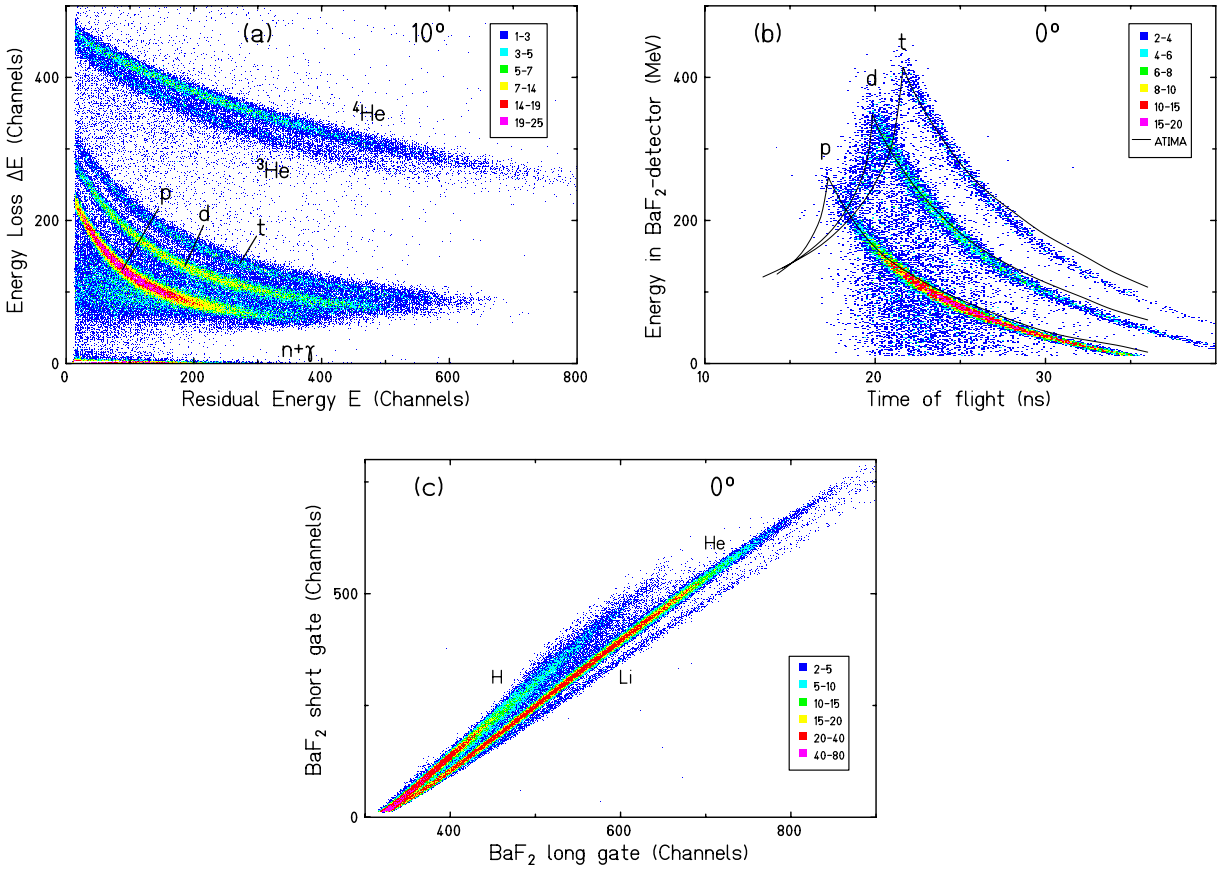

Figure 4. Examples illustrating the data analysis. (a) Correlation of energy loss and residual energy measured with the $\Delta E - E$ telescope detector. Hydrogen and helium isotopes can be well separated as can neutrons which do not give a signal in the ΔE-detector. (b) Correlation of particle energy deposited in the BaF_2-detector and the time-of-flight showing typical escape events at high energies. The solid lines represent simplified ATIMA calculations. (c) Short-gate versus long-gate integration of the BaF_2 signal.

2.2. Fragment detection and identification

Nuclear fragments emerging from the water target were detected with a $\Delta E - E$-telescope placed at a distance of 3.05 m (target centre to telescope entrance) and horizontal angles between 0° and 30° with respect to the beam axis. The angles are referenced to a spherical coordinate system with its origin at the centre of the target. The telescope consisted of two different scintillation detectors. The energy loss ΔE of charged particles was measured by a 9 mm thick NE102 scintillator paddle with a hexagonal shape and an inscribed radius of 5.4 cm. It was coupled through a light guide to an EMI 9954 QB photomultiplier. The total energy E of charged particles was measured by stopping the particles in a 14 cm long BaF_2 crystal. Protons are stopped up to energies of 250 MeV. The BaF_2 crystal was also hexagonally shaped with an inscribed radius of 4.5 cm and directly coupled to a Thorn EMI 9821 QB photomultiplier. By combining the coincident signals from the two detectors the nuclear charge Z and mass number A of charged fragments were identified from two-dimensional $\Delta E - E$ plots (figure 4).

The kinetic energy of the fragments (both charged particles and neutrons) was obtained from time-of-flight measurements. The start and stop signals were derived from the beam counting scintillator S1 and the BaF_2 detector, respectively.

The ΔE-detector has very small detection efficiency for neutrons while charged particles passing through the detector are registered with practically 100% efficiency. Therefore, it was used to discriminate neutrons from charged particles by generating a veto signal which was processed in the data acquisition electronics.

The response of the BaF_2 scintillation detector to fast neutrons was investigated in separate measurements [22] performed at the neutron beam facilities of the Université Catholique de Louvain (UCL) in Belgium and of the iThemba LABS in South Africa. The detector was exposed to calibrated quasi-monoenergetic neutron fields in the energy range of 45–198 MeV. The neutron efficiency of the detector was found to be 7% at 45 MeV and reaches a plateau value of 17% between 100 and 198 MeV.

2.3. Electronics and data acquisition

The data were recorded in list-mode event-by-event using the CAMAC data acquisition system MBS [23]. The trigger for the data acquisition required the coincident detection of a primary beam particle in S1 and of a fragment signal in the BaF_2 detector, which was verified by a hardware coincidence unit. The anode signals of the three scintillation detectors were fed into constant-fraction discriminators (CFD GSI-CF8000, NIM), and into charge-to-digital-converters (QDC LRS2249A, CAMAC), where the signals were integrated over a 50 ns gate. In addition, the anode signal of the BaF_2 detector was integrated in a second QDC over 1 μs for pulse-shape discrimination. The time-of-flight data were recorded by a time-to-digital-converter (TDC LRS2228A, CAMAC). The average dead-time in each measurement was obtained by comparing the actual number of events recorded by the data-acquisition system to the number of trigger pulses.

2.4. Data analysis

The two-dimensional $\Delta E - E$ scatter plots shown in figure 4 illustrate the fragment identification and show the clear separation of hydrogen and helium fragments. Events with very small or no ΔE-signal correspond to neutrons or photons. Protons, deuterons and tritons and the isotopes ^{3}He and ^{4}He can be well resolved as long as they are completely stopped in the BaF_2 detector. At small angles (0°, 5° and 10°), the most energetic hydrogen fragments pass through the detector and appear as escape events on the down-bending left branch below the maximum energy deposition in the E-TOF diagram (figure 4(b)). The graphical separation of fragments for further analysis was performed by first selecting a group of fragments (e.g. hydrogen or helium) by polygonal conditions in the $\Delta E - E$ diagrams and generating the corresponding E-TOF diagram. Then conditions on individual fragments (n, p, d, t, ^{3}He and ^{4}He) were defined in the E-TOF diagram and the related time-of-flight spectra were generated. As can be seen from figure 4(b) deuterons and tritons cannot be separated in those regions at high energies where their escape events are overlapping. It was shown by Kurosawa *et al* [17] that overlapping escape events can be separated by using short and long gates for integration of the output signals of an NE213 liquid scintillation detector. For the BaF_2 detector used in the present measurements, the plot of short-gate versus long-gate integration (figure 4(c)) gives a

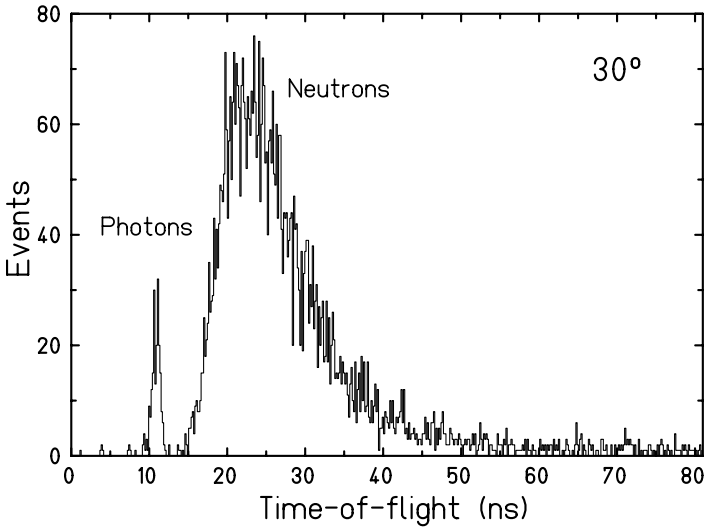

Figure 5. The time-of-flight spectrum of neutral events recorded at $\theta = 30°$. The position of the photon peak was used for absolute time calibration.

clear separation of hydrogen, helium and lithium fragments, but the resolution is not sufficient for separating protons, deuterons and tritons.

2.5. Analysis of time-of-flight data

In the time-of-flight spectra of neutral events (figure 5), a prompt photon peak is observed corresponding to a flight time of 10.7 ns, which is clearly separated from the broad time distribution of neutrons. The position of the prompt photon peak was used to identify the time-zero channel for the absolute time calibration. The neutron time-of-flight spectra were converted into energy spectra using the relativistic energy relations:

$$E = \gamma m_0 c^2 \quad \text{and} \quad E = m_0 c^2 + E_{\text{kin}},$$

where E is the total energy of the neutron, E_{kin} its kinetic energy, $m_0 c^2$ its mass at rest and γ the relativistic factor. The relative velocity β is a function of the length of the flight path l and the time-of-flight t:

$$\beta = l/(tc).$$

The kinetic energy as a function of the time-of-flight is given by:

$$E_{\text{kin}} = \left(\frac{1}{\sqrt{1 - (l/(tc))^2}} - 1 \right) m_0 c^2.$$

For the calculation of energy distributions from time-of-flight data the relative energy resolution given by the gaussian error propagation has to be considered:

$$\frac{\Delta E}{E} = -\gamma(\gamma + 1)\frac{\Delta t}{t}.$$

The time resolution of $\Delta t = 0.8$ ns was taken from the observed FWHM of the prompt gamma-peak in the time-of-flight spectra of neutral particles. As Δt is considered to be constant and independent of the time-of-flight t, the relative energy resolution $\Delta E/E$ is not constant, i.e. the constant time bins of the time-of-flight spectra are transformed into energy bins of varying bin size depending on the time t.

The measured time-of-flight is given by

$$t_{\mathrm{meas}} = t_{\mathrm{p}} + t,$$

where t_{p} is the time passing from detection of a primary ^{12}C ion in the start detector S1 till occurrence of the fragmentation reaction in the water target, and t is the time needed by the neutron to travel from the reaction point to the BaF_2 stop detector. For the time-to-energy conversion the simplifying assumption was made that the nuclear fragmentation reaction occurs at half of the mean range R (see figure 3) of the primary 200 MeV u^{-1} ^{12}C ions in the water target. The time t_{p} was calculated to be 0.84 ns, using the stopping power code ATIMA [21]. This assumption implies an uncertainty on the time–energy conversion and on the particle fluence as the fragmentation reaction can occur with about equal probability at any depth between target entrance and end of range of the primary ion. Thus, the remaining water thickness which is penetrated by the fragment varies between L_{W} (the total thickness of the water target) and $L_{\mathrm{W}} - R$, and correspondingly affects the fragment's energy loss and absorption.

The main contribution to absorption of fast neutrons in water comes from collisions with ^{16}O nuclei with a mean cross section of 295 mb ($E_{\mathrm{n}} = 100$–150 MeV) [24], corresponding to a mean free path of about 1 m. The fraction of neutrons lost by absorption in the water target is then estimated as 4%–12% assuming production at the end of range of the carbon beam or at target entrance, respectively. The corresponding difference in time-of-flight is 0.55 ns for 30 MeV neutrons and 0.11 ns for 200 MeV neutrons, which is below the time resolution of 0.8 ns. As about 90% of the neutrons pass through the water target without interaction the deceleration of neutrons in the target was assumed to be negligible. The measured yields given in this work refer to neutrons observed at the target exit.

In contrast to fast neutrons charged particles suffer significant energy losses in all material which is traversed on their way from the point of creation to detection in the BaF_2 crystal. For each isotope (p, d, t, ^{3}He and ^{4}He), the correlation between particle energy (referred to BaF_2 entrance) and t_{meas} was calculated with the ATIMA code [21], taking into account the energy loss of charged fragments in the water target from $R/2$ up to the end of the water target, along the flight path in air, in the ΔE-detector and in the cover plate of the BaF_2-detector (1 mm Al).

As shown above, at small angles (0°–10°) the most energetic deuterons and tritons are not completely stopped in the BaF_2 detector. Therefore, at specific energies above 150 MeV u^{-1} the gate condition on deuterons includes also triton events clearly visible as a bump in this part of the spectrum. An example is shown in figure 6.

3. Results

3.1. Neutron energy spectra

Neutron energy spectra ($E_{\mathrm{n}} > 20$ MeV) measured at laboratory angles of 0°, 10°, 20° and 30° behind the thick water target are shown in figure 7. It should be noted that these 'effective' spectra include neutrons produced in the target by interactions of primary ions as well as

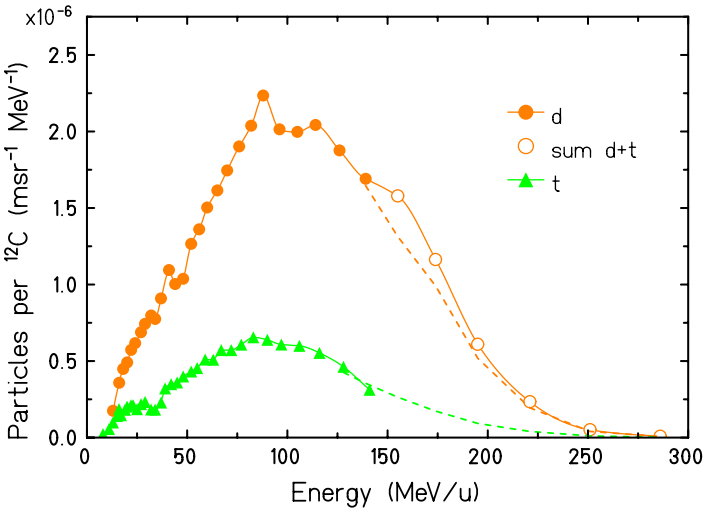

Figure 6. Energy spectra of secondary deuterons (d) and tritons (t) at 0°. The bump in the deuteron spectrum (open symbols) at specific energies above 150 MeV u^{-1} is caused by a triton contribution which could not be separated in the data analysis. The dashed lines indicate an estimated decomposition of the data in this part.

by interactions of secondary particles and imply scattering and attenuation effects due to the passage of particles through the thick water target.

At small angles, the energy distributions have a broad maximum at about half of the projectiles energy per nucleon. This maximum is related to the beam energy since the neutrons emitted at small angles are mostly produced by projectile abrasion, i.e. these neutrons have energies close to the beam energy at the moment of the nuclear interaction and are therefore sharply forward peaked. At larger angles, the neutron emission becomes less forward peaked due to the more isotropic character of the evaporation process. The exponential shape of the energy spectra at high energies is characteristic for nucleons ablated from highly excited nuclear structures like the fireball and projectile pre-fragments. The maximum neutron energy extends to almost twice the energy of the projectile per nucleon which can be explained by the transfer of the Fermi-momentum of target nucleons during the collision [25]. The neutron spectra obtained at 0° and 30° are compared in figure 7 with thick-target data reported by Kurosawa *et al* [16] and Cecil *et al* [15]. The experimental conditions of various thick-target datasets using ^{12}C beams and/or water targets are compiled in table 1.

For comparison of these data the different projectile/target combinations, the fraction f_{nucl} of ions undergoing nuclear interactions and the transport of the neutrons through the thick-target have to be taken into account. The factor f_{nucl} in table 1 was calculated as

$$f_{\mathrm{nucl}} = 1 - \exp(-R/\lambda_{\mathrm{abs}}),$$

where λ_{abs}, the mean free path length in the thick target, was taken from [6] for ^{12}C in water and from [26] for the other projectile/target combinations and was assumed to be energy-independent. Kurosawa *et al* [16] used primary ^{12}C ions at nearly the same energy per nucleon but a thick graphite target instead of water. In comparison with our data, the neutron yields at

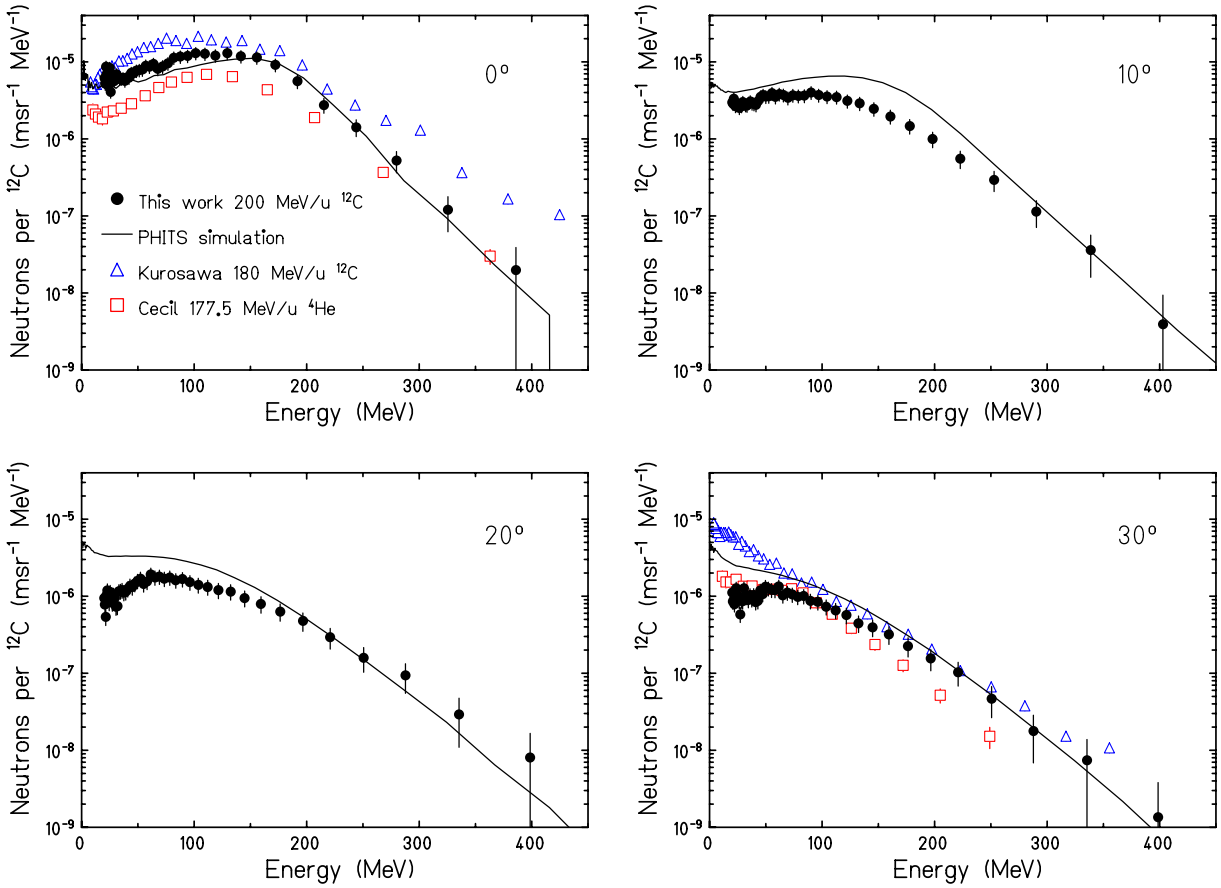

Figure 7. Neutron energy spectra measured at laboratory angles of 0°, 10°, 20° and 30° (full symbols) compared with PHITS simulations (solid lines). Each data point corresponds to an energy bin extending halfway to the neighbouring points. At 0° and 30° the energy spectra measured by Kurosawa *et al* [16, 17] and by Cecil *et al* [15] are displayed for comparison (open symbols).

0° are larger by about a factor of two. Cecil *et al* [15] used a thick water target as in this work, but ^{4}He as primary ions. In this case, one would expect much lower neutron yields because of the smaller number of neutrons in the projectile, a smaller value of f_{nucl} and the high-nuclear-binding energy of ^{4}He. This is, however, partly compensated by the ratio R/d of ion beam range and target thickness which was 0.92 in [15] compared to 0.67 in this work. The lowest yield was observed in [18] in accordance with the lowest value of f_{nucl} in table 1. The correlation of the neutron yield with f_{nucl} is shown in figure 8.

3.2. Charged-particle spectra

The energy spectra for secondary charged particles obtained from the time-of-flight data are shown in figure 9 for hydrogen isotopes and in figure 10 for ^{3}He and ^{4}He. The lower cut-off energy in the charged-particle spectra reflects the lower threshold setting of the fast discriminator processing the signals of the BaF_2-detector. For protons and α-particles the minimum energies at the exit of the water target required for detection in the BaF_2-scintillator

Table 1. Comparison of experimental conditions of various thick-target experiments.

	This work	Kurosawa [16]	Heilbronn [18]	Cecil [15]
Primary ion	^{12}C	^{12}C	^{12}C	^{4}He
Energy (MeV u^{-1})	200	180	155	177.5
Target material	Water	Graphite	Aluminium	Water
Target thickness d (g cm^{-2})	12.78	10.62	22.30	22.9
Ion beam range R (g cm^{-2})	8.58	8.10	7.18	21.00
Ratio R/d	0.67	0.76	0.32	0.92
Nuclear interactions f_{nucl}	27%	30%	18%	23%
Neutron yield	0.54	0.8	0.179	0.48

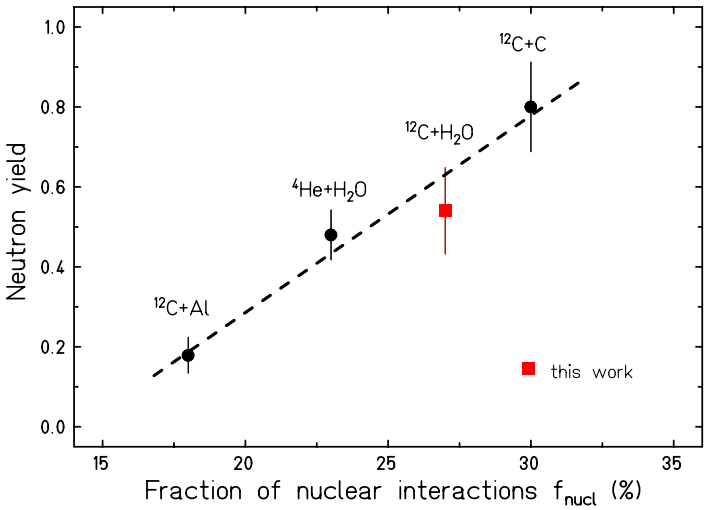

Figure 8. Measured neutron yields from [15]–[18] and this work versus the fraction f_{nucl} of ions undergoing nuclear interactions in the target (see table 1).

is 42 MeV u^{-1}. Heavier projectile-like fragments (lithium, beryllium and boron nuclei) have shorter ranges and are stopped within the water target. The shapes of the proton and neutron energy spectra are similar at all angles. The spectra extend to about 400 MeV u^{-1}, i.e. twice the energy per nucleon of the primary ions. The spectra of heavier fragments exhibit a broad maximum at about 100 MeV u^{-1} and extend only up to 200 MeV u^{-1}, in contrast to the neutron and proton spectra. Thus, the transfer of Fermi-momentum seems to be of minor importance for heavier fragments.

3.3. Angular distributions and yields

The angular distributions $f(\theta)$ of secondary fragments (figure 11) were obtained by integrating the energy spectra. They are all forward peaked and much broader than the angular definition of the primary ^{12}C beam. The profile of the primary beam, measured without water target at the

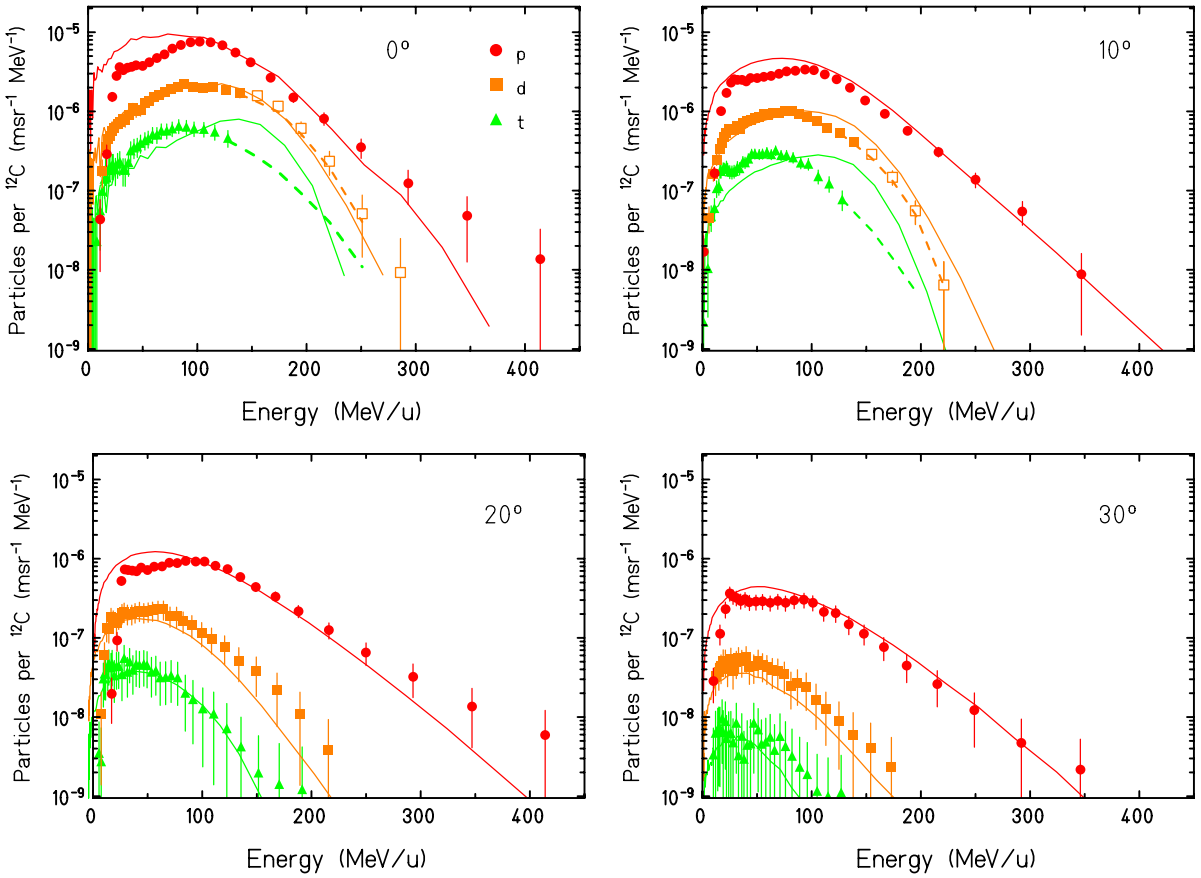

Figure 9. Energy spectra of secondary protons, deuterons and tritons measured at forward angles from 0° to 30°. The data are compared with simulations of the Monte-Carlo code PHITS (solid lines). At small angles and energies above 150 MeV u^{-1} the deuteron spectrum (open squares) contains small contributions from tritons. The dashed lines indicate an estimated decomposition (see also figure 6).

position of the detector telescope, had a width of 16 mm FWHM, corresponding to $\sigma_\theta = 0.64°$. This is mainly due to scattering in the vacuum exit window, the start detector S1 and along the 3 m air path.

The observed angular distributions include the fragmentation process itself as well as multiple scattering and absorption processes of the fragments in the target material. Helium fragments are strongly forward peaked, while hydrogen fragments and neutrons show a broader angular distribution. They are frequently produced by evaporation, where they are emitted isotropically in the centre-of-mass system of the evaporating nuclei.

Measured half-widths at half maximum are given in table 2. At forward angles from 0° to about 10° the angular distributions of all fragments are well described by Gaussian functions, at larger angles exponential functions give a better fit. Fragment yields in the forward hemisphere Y_{forw} were obtained by integration of $f(\theta)$ over $\theta = 0°$–$90°$, extrapolating the exponential functions which were fitted to the data up to 30°. This includes all observed fragments with

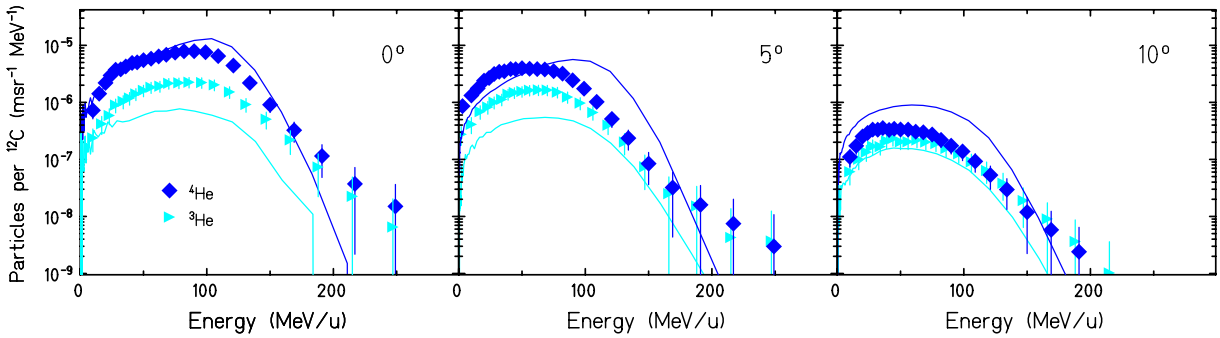

Figure 10. Energy spectra of secondary ^{3}He and ^{4}He isotopes measured at forward angles from 0° to 10°. The data are compared with simulations of the Monte-Carlo code PHITS (solid lines).

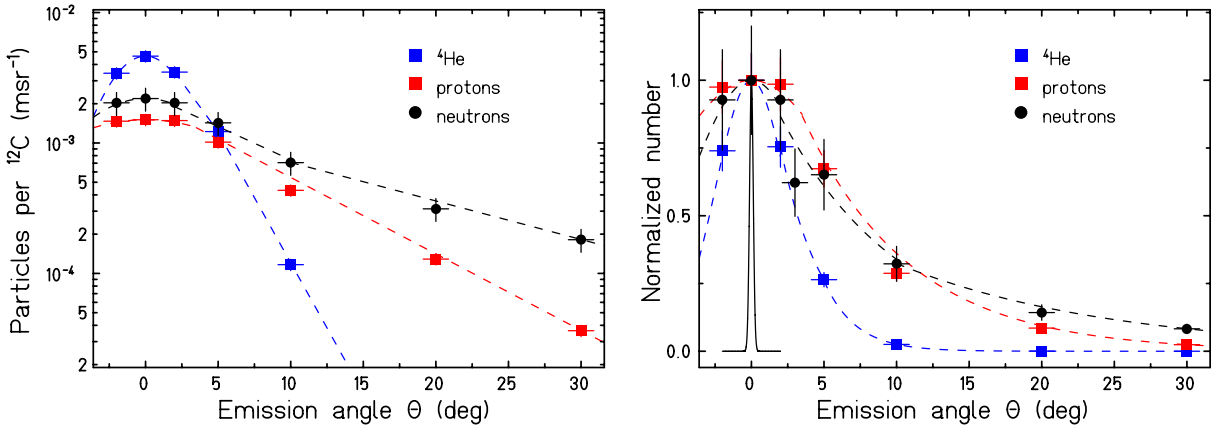

Figure 11. Angular distributions of secondary fragments measured at forward angles from −2° to 30° (left) and normalized distributions (right). The profile of the primary ^{12}C beam at the position of the fragment detector and without water target is shown for comparison (solid line). The dashed lines represent fit curves using Gaussian plus exponential functions.

Table 2. Angular widths and forward yields of secondary fragments.

	n	p	d	t	^{3}He	^{4}He
Half-width at half maximum	7.0°	6.7°	6.7°	6.6°	4.2°	3.1°
Forward yield	0.54(11)	0.20(3)	0.08(1)	0.030(5)	0.030(5)	0.09(1)

energies above 20 MeV u^{-1}

$$Y_{\text{forw}} = 2\pi \int_0^{90^\circ} f(\theta)\sin(\theta)\,\mathrm{d}\theta$$

The neutron angular distribution was fitted by a Gaussian function (0°–2°) and two different exponential functions (2°–10° and 10°–30°). The solid angle which covers 90% of the forward yield corresponds to emission angles θ of ±60° for neutrons, but only ±10° for ^{4}He particles.

4. PHITS Monte Carlo simulations

In figures 7, 9 and 10, the experimental neutron and charged-particle spectra are compared to Monte-Carlo calculations performed with the PHITS code [27]. The physical processes included in PHITS can be schematically divided into collision and transport processes. Transport calculations are supported for neutrons (1E-5 eV to 200 GeV), protons, mesons and baryons (0–200 GeV), nuclei (0–3 AGeV) and photons and electrons (1 keV to 1 GeV).

For the atomic and nuclear reactions in water different models are used in PHITS. Total reaction cross sections of the projectile (and produced fragments) in water for different energies were obtained from the semi-empirical model by Tripathi *et al* [26], dE/dx and energy- and angular-stragglings are calculated by the ATIMA code [21]. Nuclear collisions of the projectile, fragments and target nuclei were simulated by the quantum molecular dynamics model JQMD [28]. The evaporation process for excited nuclei after the JQMD calculation was treated by the GEM model [29]. All the produced fragments were followed up and further reactions were treated by the same methods as given above.

The calculations were done in a three-dimensional space. Beam and target characteristics and geometries used in our experimental set-up were exactly reconstructed for the simulations. The calculated fragment velocities refer to the entrance surface of the BaF_2-crystal.

In order to increase statistics for fragment detections, the calculations were not done for the real detector geometry. Instead, the fragment events were calculated for a ring-shaped solid angle defined by the overlap of a sphere of radius 305 cm (the distance between target centre and detector) and two cones with angles of $\theta \pm \Delta\theta$, where $\Delta\theta$ is the opening angle corresponding to the edge of the BaF_2 detector entrance surface (e.g. 9.143 and 10.847 for the measurement at 10°, where $\Delta\theta = 0.847°$). Numbers of encountered fragments were scored for different velocities. The obtained energy histograms were normalized to the number of incident ^{12}C beam particles and divided by the energy bin size and the solid angle segment $\Delta\Omega = 2\pi(\cos(\theta - \Delta\theta) - \cos(\theta + \Delta\theta))$.

The gross shape of the neutron spectra shown in figure 7 is well reproduced by the PHITS calculations. At 0° the calculated neutron yields are about 40% lower than the experimental ones, while at larger angles the broad peak seems to be more pronounced and the calculated yields slightly overestimate the data. The experimental data for charged fragments (figures 9 and 10) are very well reproduced for protons and deuterons, but show larger deviations for the triton and helium data. These differences might be explained by nucleon clustering effects, which are not included in the actual version of the PHITS code.

The neutron detection threshold in our measurements was about 20 MeV. Below this energy the detection efficiency of the BaF_2 detector becomes very small and uncertain. In order to estimate the fraction of neutrons below the experimental threshold, neutron energy spectra were simulated with PHITS for different angles down to very low energies (figure 12). From these calculations, the fraction of neutrons below 20 MeV was found to be 2.3% at 0° and 14.3% at 30°.

5. Estimated neutron dose and comparison with direct dose measurements

An estimate of the neutron equivalent dose was obtained by convolution of the measured neutron fluences (figure 7) with the ambient dose equivalent $h^*(10)$ [30, 31]. The resulting neutron dose angular distribution at 3 m distance downstream of the beam-stopping target is shown in

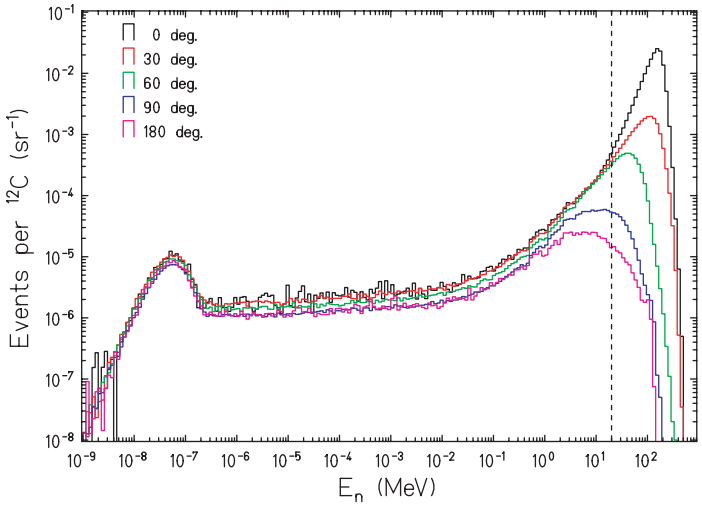

Figure 12. Energy spectrum of secondary neutrons simulated with PHITS for the conditions in this experiment. Note that the data are given in units of sr^{-1}, i.e. not divided by the energy bin as in figure 7. The experimental detection threshold energy of 20 MeV is indicated by the dashed line.

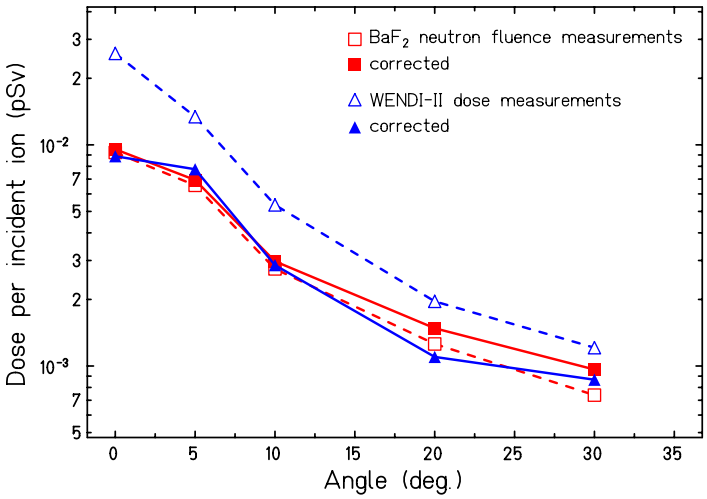

Figure 13. Neutron dose angular distributions for 200 MeV u^{-1} ^{12}C ions stopping in a 12.8 cm thick water target. Neutron doses at 3 m distance from the target were obtained by convolution of neutron fluences measured with a BaF_2 detector with the ambient dose equivalent $h^*(10)$. For comparison direct neutron dose measurements [32] using a WENDI-II detector are shown.

figure 13. The maximum dose at 0° is about 10^{-2} pSv per incident ^{12}C, at 30° the dose is a factor of 10 lower.

These neutron dose values derived from measured neutron fluences can be compared to neutron doses obtained directly from a neutron dose meter. Such measurements were performed recently by Iwase *et al* [32] under identical experimental conditions (beam and water target)

as in this work, but replacing the BaF_2 telescope detector by a wide-energy-neutron detector (WENDI-II [33]). This neutron dose meter was designed so that its response per unit fluence approximates the fluence-to-dose conversion function and additionally covers a wide range of neutron energies from thermal up to gigaelectronvolt. This special feature is important for comparing with our fluence data with neutron energies extending up to 400 MeV, while the response of standard neutron dose meters drops down rapidly beyond 10 MeV.

However, the apparent neutron dose obtained from the WENDI-II detector has still to be corrected for significant contributions caused by high-energy charged particles, mainly protons and α-particles occurring with similar intensities in the secondary particle field. As shown in [32], the response of WENDI-II to charged particles is negligible up to energies of about 100 MeV, but then increases steeply for higher energies. After correcting the dose values measured with WENDI-II for the charged-particle contributions, good agreement was found with the neutron doses obtained from the BaF_2 fluence data (figure 13). The BaF_2 data points include a correction for neutrons below the detection threshold of 20 MeV.

6. Dose contributions of secondary fragments in carbon ion treatments

6.1. Fast neutrons

Based on the measured neutron yield for 200 MeV u^{-1} ^{12}C ions stopping in water the dose contribution of secondary fast neutrons in patient treatments with carbon ions was estimated by converting the neutron fluence into kerma (kinetic energy released per mass unit). As a typical treatment volume the irradiation of a cube with the side length of 5 cm, i.e. an irradiated area of 25 cm^2, was assumed. To apply 20 Gy absorbed dose (corresponding to about 60 GyE biologically effective dose) to the given volume, a total amount of 5×10^{10} carbon ions is required. This number is obtained from the computer code TRiP [7, 8] which is routinely used for patient treatment planning at GSI. The biologically effective dose given in units of cobalt gray equivalent (GyE) includes the RBE of the particles. Because of the complex composition of the particle field due to nuclear fragmentation, however, the biologically effective dose is not a simple product of absorbed dose and a mean RBE value but is evaluated by an iterative procedure using the TRiP code.

Taking the measured neutron yield of 0.54 ion^{-1}, the neutron fluence at a distance of 4 cm behind the irradiated volume then amounts to $(1.1 \pm 0.4) \times 10^9$ neutrons cm^{-2}. (This distance corresponds to the difference of target thickness and ion beam range in our measurements.) The kerma coefficient in water recommended in [24] was extrapolated to a neutron energy of 200 MeV ($k = 150$ pGy cm^2) and multiplied with the fluence Φ(E) to obtain the neutron kerma. The resulting neutron dose of 162 mGy/20 Gy or 8 mGy per treatment-Gy is less then 1% of the treatment dose. This result is in good agreement with recent calculations [34] based on the Monte-Carlo code GEANT4.

Alternatively, the neutron equivalent dose (as defined in health physics) can be estimated by multiplying the neutron fluence with the conversion coefficient $h_\Phi(E)$. Using a mean value of $h_\Phi = 300$ pSv cm^2 [35] we obtain a dose of 16 mSv per treatment-Gy, corresponding to 5.4 mSv per treatment-GyE.

Table 3. Comparison of neutron yields and neutron dose in ^{12}C ion- and proton-radiotherapy for scanning beam delivery systems.

	Beam (MeV u^{-1})	Target (g cm^{-2})	Neutrons per primary ion	Neutron dose[b] (mSv per treatment-GyE)
This work	^{12}C (200)	H_2O (12.78)	$0.54 \pm 20\%$	$5.4 \pm 20\%$ (scanning)
Schneider [36]	p (177)	H_2O (30.1)	(0.025)[a]	$2.3 \pm 30\%$ (scanning)

[a] Recalculated from the dose given in [36].
[b] Dose expected in normal tissue of the patient in the non-treated volume for a medium-sized target.

6.2. Charged particles

The absorbed dose D produced by a parallel beam of directly ionizing charged fragments with a specific energy loss $\mathrm{d}E/\mathrm{d}x$ in a medium is given by

$$D(\mathrm{Gy}) = 1.602 \times 10^{-9} \times F \frac{\mathrm{d}E}{\mathrm{d}x} \frac{1}{\rho},$$

where $F(\mathrm{cm}^{-2})$ is the particle fluence and $\rho(\mathrm{g\,cm}^{-3})$ the mass density of the medium. As can be seen from the PHITS calculation shown in figure 1, the dose tail which is caused entirely by beam fragments is a complex superposition of the contributions of different fragments with nuclear charges from $Z = 5$ (boron) down to $Z = 1$ (hydrogen). Just behind the Bragg peak, boron fragments give the major contribution until they are slowed down. At larger depths hydrogen and helium fragments which have the longest stopping ranges produce most of the dose tail.

A similar dose estimate as given above for fast neutrons, can be obtained from the yields for hydrogen and helium fragments given in table 2 and applying the above fluence-dose relation. Using a mean value of 100 MeV u^{-1} for the specific energy of both hydrogen (H) and helium (He) fragments (see figures 9 and 10) the corresponding $\mathrm{d}E/\mathrm{d}x$ values were calculated with the ATIMA-code as 0.73 keV μm^{-1}(H) and 2.95 keV μm^{-1}(He). The resulting dose values are $D_\mathrm{H} = 36$ mGy per treatment-Gy and $D_\mathrm{He} = 58$ mGy per treatment-Gy. Again, this represents a rough approximation of the doses at 4 cm distance behind the Bragg peak of 200 MeV u^{-1} ^{12}C ions. The ratio $D_\mathrm{H}/D_\mathrm{He} = 0.62$ compares to 0.42 in the PHITS calculation (figure 1).

Comparing now the estimated dose contributions of charged particles ($36 + 58 = 94$ mGy per treatment-Gy) and fast neutrons (8 mGy per treatment-Gy), the above simple approximations suggest that the neutron dose is more than a factor of 10 lower than the dose caused by charged fragments.

6.3. Comparison of neutron doses in proton and carbon ion therapy

In table 3, dose contributions of secondary neutrons obtained in the present work with ^{12}C ions at GSI and from measurements at the proton therapy facility at PSI (Switzerland) [36] are compared. Both the treatment units use scanning beam delivery systems. Although the yield of fast neutrons is much higher for ^{12}C ions than for protons the neutron doses per treatment-GyE

are not very different due to the fact that a much lower number of ^{12}C ions is needed to produce the same biologically effective dose as protons. (The dose scales with dE/dx, where the nuclear charge of the projectile enters as Z^2 and there is an additional gain for carbon ions due to their elevated RBE-factor).

For passive beam delivery systems, where secondary neutrons are produced mainly by interactions of the primary beam with collimators, range shifters and other elements located in front of the patients, the neutron dose varies significantly with the configuration of the beam modifying equipment. This was examined experimentally by Yan *et al* [37] for the medical beam line at the Harvard Cyclotron Laboratory. They found neutron dose equivalent values of typically 1–5 mSv Gy^{-1} at 50 cm distance from the isocenter.

Monte-Carlo calculations performed by Agosteo *et al* [38] for the proton therapy beam lines at PSI (active scanning) and at iThemba LABS South Africa (passive system) confirm the experimental results by Schneider *et al* [36] and Binns and Hough [39]. For the passive beam delivery system the calculated secondary neutron dose is ten times higher which seems to originate predominantly from neutrons generated in the last collimator.

7. Conclusion

Properties of secondary particles produced in fragmentation reactions of high-energy carbon ions beams with tissue-like material (water) were investigated experimentally by measuring their energy spectra, angular distributions and yields. The energy of 200 MeV u^{-1} of the incident ^{12}C ions and the thickness of the water absorber (12.8 cm) used in our measurements are representative for the treatment of deep-seated medium-sized tumours in the head/neck-region as treated at the carbon ion facility at GSI Darmstadt.

Secondary fragments are produced continuously along the penetration path and exhibit wide energy spectra. Fast neutrons are produced with energies up to about twice the specific energy of the primary carbon ions. The experimental energy spectra of neutrons and protons can be fairly well-reproduced by the Monte-Carlo code PHITS, while some discrepancies were found for triton and helium spectra at small angles.

Hydrogen and helium fragments have the longest ranges and mainly cause the long dose tail behind the Bragg peak. These fragments are emitted in a rather narrow cone in forward direction, while protons and neutrons show about twice the angular width of helium fragments.

The dose contribution caused by secondary neutrons in carbon ion radiotherapy, estimated on the basis of the measured neutron yield, is of the order of 1% of the treatment dose and is much lower than the dose caused by secondary charged fragments. Further measurements as well as Monte-Carlo calculations are planned to investigate the dose deposition of secondary fragments, in particular in regions outside of the planned treatment volume.

Acknowledgments

We thank Gerhard Kraft (GSI) for his continuous support of these experiments and many stimulating and encouraging discussions. Furthermore, we thank Volker Dangendorf and Ralf Nolte, PTB Braunschweig, for excellent collaboration and invaluable support during the neutron efficiency measurements in Louvain-la-Neuve and Cape Town.

References

[1] Kraft G 2000 Tumor therapy with heavy charged particles *Prog. Part. Nucl. Phys.* **45** S473–544

[2] Tsujii H *et al* 2004 Overview of clinical experiences on carbon ion radiotherapy at NIRS *Radiother. Oncol.* **73** S41–9

[3] Schulz-Ertner D *et al* 2004 Results of carbon ion radiotherapy in 152 patients *Int. J. Radiat. Oncol. Biol. Phys.* **58** 631–40

Nikoghosysan A *et al* 2004 Evaluation of therapeutic potential of heavy ion therapy for patients with locally advanced prostate cancer *Int. J. Radiat. Oncol. Biol. Phys.* **58** 89–97

Schulz-Ertner A *et al* 2005 Therapy strategies for locally advanced adenoid cystic carcinomas using modern radiation therapy techniques *Cancer* **104** 338–44

[4] Serber R 1947 Nuclear reactions at high energies *Phys. Rev.* **72** 1114–5

[5] Schardt D, Steidl P, Krämer M, Weber U, Parodi K and Brons S 2008 *GSI Scientific Report 2007* in preparation

[6] Sihver L, Schardt D and Kanai T 1998 Depth-dose distributions of high-energy carbon, oxygen and neon beams in water *Japan. J. Med. Phys.* **18** 1–21

[7] Krämer M, Jäkel O, Haberer T, Kraft G, Schardt D and Weber U 2000 Treatment planning for heavy-ion radiotherapy: physical beam model and dose optimization *Phys. Med. Biol.* **45** 3299–317

[8] Krämer M and Scholz M 2000 Treatment planning for heavy-ion radiotherapy: calculation and optimization of biologically effective dose *Phys. Med. Biol* **45** 3319–30

[9] Schimmerling W, Vosburgh K and Todd P 1971 Interaction of 3.9 GeV nitrogen ions with matter *Science* **174** 1123–5

[10] Schimmerling W, Miller J, Wong M, Rapkin M, Howard J, Spieler H G and Jarret B V 1989 The fragmentation of 670 MeV/u neon-20 as a function of depth in water *Radiat. Res.* **120** 36–71

[11] Schall I *et al* 1996 Charge-changing nuclear reactions of relativistic light-ion beams ($56 \leqslant Z \leqslant 10$) passing through thick absorbers *Nucl. Instrum. Methods Phys. Res.* B **117** 221–34

[12] Golovkov M, Aleksandrov D, Chulkov L, Kraus G and Schardt D *et al* 1997 Fragmentation of 270 MeV/u carbon ions in water *Advances in Hadrontherapy* (*Excerpta Medica International Congress Series vol 1144*) ed U Amaldi, B Larsson and Y Lemoigne (Amsterdam: Elsevier) p 316

[13] Matsufuji N *et al* 2003 Influence of fragment reaction of relativistic heavy charged particles on heavy-ion radiotherapy *Phys. Med. Biol.* **48** 1605–23

[14] Matsufuji N *et al* 2005 Spatial fragment distribution from a therapeutic pencil-like carbon beam in water *Phys. Med. Biol.* **50** 3393–403

[15] Cecil R *et al* 1980 Neutron angular and energy distribution from 710 MeV alphas stopping in water, carbon, steel and lead and 640 MeV alphas stopping in lead *Phys. Rev.* C **21** 2471–84

[16] Kurosawa T *et al* 1999 Measurements of secondary neutrons produced from thick targets bombarded by high-energy helium and carbon ions *Nucl. Sci. Eng.* C **132** 30–56

[17] Kurosawa T *et al* 1999 Spectral measurements of neutrons, protons, deuterons, tritons produced by 100 MeV/nucleon He ion *Nucl. Instrum. Methods Phys. Res.* A **430** 400–22

[18] Heilbronn L *et al* 1999 Neutron yields from 155 MeV/nucleon carbon and helium stopping in aluminium *Nucl. Sci. Eng.* **132** 1–15

[19] Gunzert-Marx K *et al* 2004 Nachweis leichter Fragmente aus Schwerionenreaktionen mit einem BaF_2-Teleskop-Detektor *PhD Thesis* (in German) Technische Universität Darmstadt, Fachbereich Physik

[20] Gunzert-Marx K, Schardt D and Simon R S *et al* 2004 Fast neutrons produced by nuclear fragmentation in treatment irradiations with ^{12}C beam *Radiat. Prot. Dosim.* **110** 595–600

[21] Scheidenberger C 1994 *PhD Thesis* Justus-Liebig-Universität Gießen
Schwab T 1991 *GSI-Report* 91-10 (see also http://www-linux.gsi.de/~weick/atima/)

[22] Gunzert-Marx K, Schardt D, Simon R S, Gutermuth F, Radon T, Dangendorf V and Nolte R 2005 Response of a BaF_2 scintillation detector to quasi-monoenergetic fast neutrons in the range of 45 to 198 MeV *Nucl. Instrum. Methods Phys. Res.* A **536** 146–53

[23] Essel H G and Kurz N 2000 The general purpose data acquisition system MBS *IEEE Trans. Nucl. Sci.* **47** 337–9
[24] ICRU 2001 Nuclear data for neutron and proton radiotherapy and for radiation protection *ICRU Report* 63
[25] Bertini H, Sanforo R and Hermann O 1976 Calculated neutron spectra at several angles from 192-, 500-, 700-, and 900-MeV ^{12}C on ^{56}Fe *Phys. Rev.* C **14** 590–5
[26] Tripathi R, Cucinotta F and Wilson J 1997 Universal parametrization of absorption cross sections *NASA Tech. Pap.* 3621
[27] Niita K, Sato T, Iwase H, Nose H, Nakashima H and Sihver L 2004 Particle and heavy ion transport code system PHITS *Proc. Symp. Nucl. Data* (*JAERI, Tokai, Japan, JAERI-Conf2004-005*) p 33
[28] Niita K, Chiba S, Maruyama T, Takada H, Fukahori T, Nakahara Y and Iwamoto A 1995 Analysis of the (N,xN′) reactions by quantum molecular dynamics plus statistical decay model *Phys. Rev.* C **52** 2620–35
[29] Furihata S 2000 Statistical analysis of light fragment production from medium energy proton-induced reactions *Nucl. Instrum. Methods Phys. Res.* B **171** 251–8
[30] ICRU 2001 Determination of Operational Dose Equivalent Quantities for Neutrons *ICRU Report 66* (Bethesda, MD: ICRU)
[31] ICRP 1997 Conversion coefficients for use in radiological protection against external radiation *ICRP Publication 74* (Amsterdam: Elsevier)
[32] Iwase H, Gunzert-Marx K, Haettner E, Schardt D, Gutermuth F, Krämer M and Kraft G 2007 Experimental and theoretical study of the neutron dose produced by carbon ion therapy beams *Radiat. Prot. Dosim.* **126** 615–8
[33] Olsher R H, Hsu H-H, Beverding A, Kleck J H, Casson W H, Vasilik D G and Devine R T 2000 WENDI: an improved neutron rem meter *Health Phys.* **79** 170–81
[34] Pshenichnov I, Mishustin I and Greiner W 2005 Neutrons from fragmentation of light nuclei in tissue-like media: a study with the GEANT4 toolkit *Phys. Med. Biol.* **50** 5493–507
[35] Ferrari A and Pelliccioni M 1998 Fluence to dose equivalent conversion data and effective quality factors for high energy neutrons *Radiat. Prot. Dosim.* **7** 215–24
[36] Schneider U, Agosteo S, Pedroni E and Besserer J 2002 Secondary neutron dose during proton therapy using spot scanning *Int. J. Radiat. Oncol. Biol. Phys.* **53** 244–51
[37] Yan X, Titt U, Koehler A M and Newhauser W D 2002 Measurement of neutron dose equivalent to proton therapy patients outside of the proton radiation field *Nucl. Instrum. Methods Phys. Res.* A **476** 429–34
[38] Agosteo S, Birattari C, Caravaggio M, Silari M and Tosi G 1998 Secondary neutron and photon dose in proton therapy *Radiother. Oncol.* **48** 293–305
[39] Binns P J and Hough J H 1997 Secondary dose exposures during 200 MeV proton therapy *Radiat. Prot. Dosim.* **70** 441–4